2025 IEEE Symposium on Diagnostics for Electric Machines, Power Electronics and Drives (SDEMPED) | 979-8-3503-8820-6/25/$31.00 ©2025 IEEE | DOI: 10.1109/SDEMPED53223.2025.11154313

Comparison of Electric Field Suppression Techniques in (U)WBG Power Modules Under Unipolar and Bipolar Square Voltages at Varying High Frequencies

Pujan Adhikari
Department of Electrical and Computer Engineering
The University of Texas at Dallas
Richardson, TX, USA
pujan.adhikari@utdallas.edu

Mona Ghassemi
Department of Electrical and Computer Engineering
The University of Texas at Dallas
Richardson, TX, USA
mona.ghassemi@utdallas.edu

***Abstract*— Most research involving resistive field grading materials or nonlinear field-dependent conductivity (FDC) layers has predominantly concentrated on DC or sinusoidal AC voltages, even though (U)WBG power electronic modules typically operate under high-frequency square wave voltages. To bridge this existing research gap, the present study systematically investigates the efficacy of an FDC coating in alleviating electric field stress when subjected to high-frequency, high-slew-rate square wave voltages. The findings indicate that applying a nonlinear FDC layer significantly reduces electric field stress, even under stringent conditions involving elevated operating frequencies. Furthermore, the influence of the square wave voltage type—the distinction between unipolar and bipolar square waveforms—on electric field stress remains inadequately understood despite substantial progress in breakdown and PD experiments related to these phenomena. Consequently, this study undertakes a comparative analysis of nonlinear FDC layers' performance under unipolar (+27.5 kV) and bipolar (±27.5 kV) square wave voltages. In doing so, this investigation contributes valuable insights into the interplay between high-frequency operation, the polarity of square waveforms, and the efficacy of nonlinear FDC layers in mitigating electric field stress within (U)WBG power module packages.**

Keywords—Field grading materials, wide bandgap power modules, Multiphysics modeling, partial discharge, electric field

I. Introduction

Power electronic modules utilizing wide bandgap (WBG) materials such as silicon carbide (SiC) and gallium nitride (GaN), alongside ultra-wide bandgap (UWBG) materials including diamond and aluminum nitride (AlN), emerge as a promising solution to achieve net-zero carbon emissions. These materials demonstrate elevated blocking voltages and enhanced performance characteristics compared to conventional silicon-based systems [1-3]. Their significance is particularly evident in their capacity to operate effectively under high slew rates (dv/dt) and to manage high-frequency repetitive voltage pulses, highlighting their potential in various power applications [4, 5]. However, transitioning to compact power modules functioning at elevated frequency voltages presents several challenges; notably, the increased electric field stress associated with this operational regime poses a considerable risk to the integrity of insulation systems within these modules [6, 7]. The triple point (TP) that occurs at the junction of the metallization layer, the substrate, and the encapsulant, along with irregularities such as protrusions along the edges of the metal, contribute to excessive electrical stresses within the power module [8-13]. These stresses can lead to the failure of the insulating materials, ceramic substrates such as AlN, and encapsulation materials such as silicone gel (SG). Several electric field mitigation strategies have been proposed to address these challenges, including geometric field control (e.g., rounding sharp corners), high-permittivity encapsulants, and materials with field-dependent permittivity or conductivity [14-17]. Among these, resistive field grading using materials with nonlinear field-dependent conductivity (FDC) has gained particular attention. These materials exhibit a nonlinear increase in conductivity with increasing electric field strength, allowing them to self-adapt and redistribute the field more uniformly across stressed regions [14, 18]. While promising, most existing work has focused on applying FDC materials under static DC or low-frequency sinusoidal voltages [19]. Their performance under fast-switching square waveforms, especially at frequencies exceeding 100 kHz, remains poorly understood [20].

Adding to this complexity is the role of voltage waveform polarity in determining insulation stress. Bipolar square voltages are known to trigger more frequent polarity reversals and charge injection cycles at dielectric interfaces, potentially aggravating space charge accumulation and interfacial degradation [21, 22]. Even when the peak-to-peak voltage, frequency, and rise time are identical, unipolar and bipolar excitations influence space charge accumulation from partial discharges (PDs) in distinct ways [23]. This often results in a significant reduction in the partial discharge inception voltage (PDIV) and a substantial acceleration of electrical tree growth under bipolar square wave voltages [24]. Some studies suggest that insulation performance deteriorates more rapidly under bipolar than unipolar square voltages due to enhanced surface tracking and electric field inversion effects [25]. However, other researchers argue that the waveform polarity has minimal impact on bulk degradation, especially when materials are tested below their PD inception threshold [26]. This lack of consensus highlights a critical knowledge gap, particularly when high-frequency, high-slew-rate square voltages are involved—conditions that increasingly characterize modern WBG-based systems. Additionally, while the presented studies investigate insulation behavior such as electrical treeing, PD, or dielectric strength under unipolar and

This work was partially funded by the U.S. National Science Foundation (NSF) under Awards 2306093 and 2401578.

bipolar pulses, a detailed analysis of the corresponding electric field distributions remains largely absent. This study aims to bridge this gap by systematically investigating the performance of nonlinear FDC layers under unipolar and bipolar square wave voltages with a fixed 175 ns rise time and 60 Hz to 500 kHz frequencies. Through detailed electric field simulations in COMSOL Multiphysics, we evaluate the impact of waveform polarity, frequency, and FDC layer placement on field stress, with a specific focus on TP and metal-edge regions. Our results reveal that bipolar square voltages induce significantly higher peak electric fields than unipolar square voltages across all frequencies. Furthermore, the field grading performance of FDC layers is found to degrade with increasing frequency, and effective mitigation is only achieved when both the high-voltage and ground electrodes are coated with the FDC layer. Additional analysis shows that increasing the substrate thickness further reduces TP stress. Overall, this work contributes novel insights into insulation design for advanced power modules by revealing the interplay between square wave polarity, frequency, and field grading material performance. These findings are highly relevant for developing robust, high-frequency (U)WBGs.

II. Simulation Model and Base Case Results

Fig. 1 shows an actual commercial power module package, and based on this, a simplified 2D model is developed in COMSOL Multiphysics (Fig. 2) to represent the essential insulation structure to facilitate clearer analysis of the electric field distribution. It consists of copper metallization layers measuring 292 µm in thickness, AlN substrate with 2.06 µm, and SG with a thickness of 4 mm encapsulating the entire structure. The substrate and gel permittivity are 9 and 2.86, respectively, and the conductivity is 10^{-11} S/m and 10^{-13} S/m. Due to imperfect brazing of metallization layers on the ceramic substrate, protrusions are formed on the edge of metallization layer, and to replicate this practical scenario, protrusions of 12 µm height and 37 µm width are also included in the model.

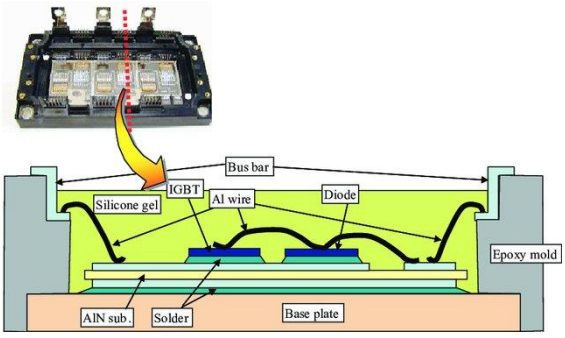

Fig 1. Schematic view of a power module package [27].

The electric field experiences significant amplification near metal edges, protrusions, and TPs. We have adopted a multi-zone meshing approach to mitigate inaccuracies in calculating electric fields. Zone 1 includes all acute edges around the metallization layer and TPs, with a maximum element size of 2 µm. Zone 2 pertains to areas adjacent to the sharp edges of the substrate and metallization layers, with a maximum element size set at 40 µm. Zone 3 encompasses regions situated farther from the edges, with a maximum element size of 400 µm. To achieve accurate measurements, measuring lines that are situated 15 µm away from the TPs are utilized. L1 corresponds to the electric field present in the SG encapsulant that surrounds the TPs of the HV electrode. Likewise, L2 illustrates the electric field within the AlN substrate. In contrast, L3 and L4 represent the electric field associated with the bottom electrode. The integration of meshing techniques with designated measuring lines facilitates precise electric field calculations, resulting in measurement errors that remain within a minimal 1%. In the context of our investigation or other simulations, the IEC 61287-1 standard specifies that a voltage of $1.1U_b$ (in our case, 27.5 kV) should be applied to the upper electrode while the lower electrode is grounded [28]. The equations used to generate the bipolar square wave pulse, along with the resulting waveform, are presented by the authors in [6]; unipolar pulses are generated similarly by modifying the control equations. 27.5 kV was selected in our study based on the envisaged 25 kV high power density SiC power modules [29, 30]. Although these modules are still in the developmental phase, this study aims to address the insulation challenges posed by the demanding operating conditions anticipated in such advanced WBG power modules. In the case of a square pulse, the electric field is affected by the instantaneous voltage, dv/dt, and the pulse's frequency. Consequently, a time-dependent solver is used with the "Electric currents (ec) module" to characterize the electric field accurately at distinct time intervals. Table I presents the electric field values measured across four distinct lines for the base case, in which a 60 Hz square wave with 175 ns rise time is applied. The electric field distribution corresponding to this scenario is illustrated in Fig. 2. As evidenced by the plot, the electric field exhibits a significant concentration in the TPs of both metallization layers, with particularly pronounced peaks observed in the TP regions of the HV electrode for both the encapsulant and substrate. This phenomenon can be attributed to the junction of three disparate materials, where the presence of sharp protrusions effectively concentrates the electric field, yielding higher values.

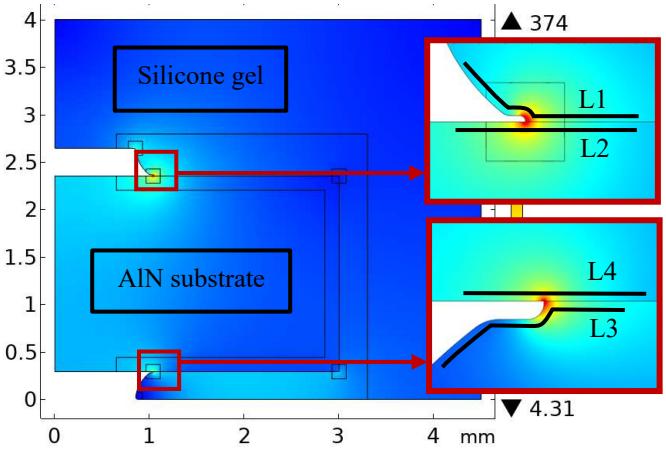

Fig 2. Electric field distribution for the base case (60 Hz).

TABLE I. Electric Field Along Lines For The Base Case

Measuring lines	L1	L2	L3	L4
E_{max} (kV/mm)	69.81	65.06	34.4	34.76

Table I reveals that the electric field intensities at the TPs of the encapsulant and substrate for the HV electrode are 102.93% and 87.17% higher than the ground electrode, respectively. In general, the electric field strength of the AlN substrate is found to range between 20-30 kV/mm, while for SG, the range is

approximately 15-20 kV/mm. When considering breakdown field strengths of 25 kV/mm for the substrate and 17 kV/mm for the SG encapsulant, it becomes evident that the electric fields along the four measuring lines exceed these thresholds significantly, measuring 310.64%, 160.24%, 102.35%, and 39.04% higher, respectively. It is important to note that in this case, and all subsequent scenarios, the square wave voltage rise time is fixed at 175 ns while the frequency is varied. As a result, the slew rate increases with frequency since the voltage must transition within the same rise time over shorter time intervals, leading to a higher rate of voltage change at higher frequencies.

III. Nonlinear Nonbridging FDC Layer Results

A field-dependent conductivity (FDC) layer, formulated by incorporating semi-conductive materials such as ZnO and SiC, represents a predominant strategy for mitigating electric field stress within (U)WBG power module packages [31, 32]. The previous section indicates that the electric field intensity is markedly elevated near HV metallization regions compared to ground areas. Consequently, this section discusses the application of an FDC layer which is strategically applied around the TP regions of the HV metallization layer and extends to the periphery of the substrate. The conductivity of the FDC layer is intrinsically linked to the intensity of the electric field; it exhibits heightened conductivity in regions experiencing elevated electric field stress, specifically around TPs and protrusions, while demonstrating reduced conductivity in areas further removed from these localized stresses. This behavior effectively contributes to attenuating the electric field in critical areas. The mathematical representation of the electric field-dependent conductivity of the FDC layer is as follows:

$$\sigma(E) = \sigma_0(1 + (E/E_b)^{\alpha-1}) \quad (1)$$

Here, σ_0 represents the low-field conductivity, E_b represents the switching field, and α represents the nonlinearity coefficient. Experiments indicate that the value of E_b should be equal to the applied voltage divided by the FDC layer length and to achieve nonlinearity even at higher frequencies, α should exceed 10 [33]. In this study, a value of 4 kV/mm is chosen for E_b initially, but is modified when the layer length is modified, with α and σ_0 as 4 and 3.3× 10^{-11} S/m.

The FDC layer is applied over the metallization to mitigate electric field stress at sharp edges and TPs without introducing additional sharp edges. To achieve this, a 100 µm-thick FDC coating is extended from the metallization to the substrate edge. Slightly increased thickness is maintained near the TPs, with the highest electric field concentration. Two specific lines, denoted as L5 and L6 in Fig. 3, are selected to quantify the electric field values along the FDC/Gel interface and the FDC/AlN interface adjacent to the HV electrode. Table II presents the corresponding electric field values associated with the nonbridging FDC layer. Given that the operational objective of the (U)WBG power modules is to function effectively at elevated frequencies, simulations were conducted across a spectrum of frequencies ranging from 60 Hz to 500 kHz. This encompassed six distinct frequency points: 60 Hz, 1 kHz, 10 kHz, 50 kHz, 100 kHz, and 500 kHz at a fixed rise time of 175ns. The 60 Hz case was selected to directly compare with traditional power frequency and highlight the significant increase in electric field stress introduced by high-frequency, fast-rise-time square voltages. This contrast emphasizes the limitations of conventional insulation studies that focus only on DC or 60 Hz AC conditions. The simulations were executed for both unipolar and bipolar square voltage inputs, allowing for an assessment of how voltage polarity influences the distribution of the electric field. Notably, the data reveals that the electric field values surrounding the TPs of the HV metallization areas, represented by lines L1 and L2, exhibit a significant reduction upon applying the FDC layer in the HV electrode regions. Conversely, the ground metallization layers observe an increase in electric field intensity. This phenomenon can be attributed to the transfer of high electric field stress from the HV electrodes to the ground electrode areas due to the implementation of the FDC layer [34].

TABLE II. Electric Field Along Lines For Section III

E_{max} (kV/mm)	Freq. (kHz)	L1	L2	L3	L4	L5	L6
Unipolar	60×10^{-3}	11.77	11.94	42.35	42.77	12.69	22.24
	1	13.23	14.36	40.9	41.31	15.45	24.1
	10	17.49	17.69	39.8	40.2	17.78	25.68
	50	18.65	19.02	38.83	39.23	19.18	26.1
	100	20.12	20.13	38.66	39.06	19.97	26.21
	500	20.89	21.82	37.95	38.34	20.89	26.48
Bipolar	60×10^{-3}	11.78	12.09	42.4	42.82	14.26	23.82
	1	13.83	15.41	40.9	41.32	16.04	25.09
	10	19.88	20.15	39.8	40.2	20.09	26.48
	50	21.18	21.74	38.95	39.35	20.89	27.38
	100	22.1	22.47	38.67	39.06	21.13	27.55
	500	22.18	22.88	37.85	38.23	22.06	27.42

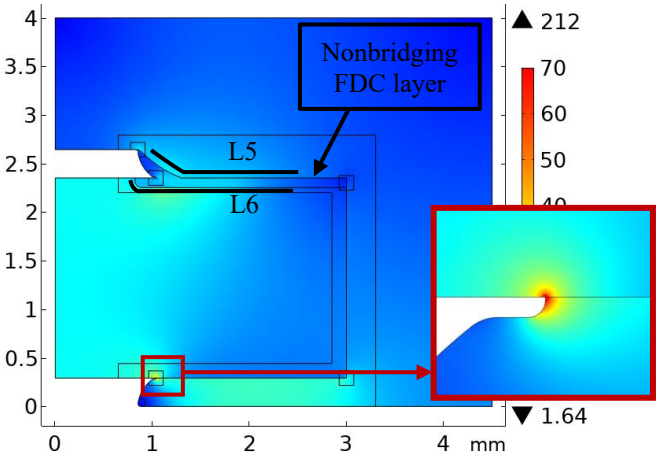

Fig 3. Electric field distribution for nonlinear nonbridging FDC layer (10 kHz).

Another critical observation is that the electric field values associated with bipolar square voltages consistently exceed those of unipolar across all frequencies. This discrepancy can be explained by the nature of the bipolar voltage, which alternates polarity between negative and positive values [35]. During simulation, there are instances wherein the voltage experiences rapid transitions from negative to positive and vice versa. Moreover, the results indicate a general trend of increasing electric field as the frequency escalates for both unipolar and bipolar cases; however, a pronounced increase in electric field is particularly evident when frequencies reach 10 kHz and above. These frequencies align with the operational range anticipated for (U)WBG power modules. Notably, beyond the threshold of 10 kHz, the electric field intensity

exhibits only marginal increases as the frequency progresses up to 500 kHz. Nonetheless, electric field values continue to ascend with higher frequencies in both conditions.

IV. Nonlinear Bridging FDC Layer Results

The preceding section noted that while the non-bridging nonlinear FDC layer effectively mitigated the electric field intensity in critical regions surrounding the HV metallization areas, a consequential increase in electric field stress in the adjacent ground regions was observed. Therefore, this section investigates the impact of extending the nonlinear FDC layer to create a bridge between the HV and ground metallization layers on the electric field intensities near the ground electrodes. Table III illustrates the electric field measurements taken across seven measurement lines (line L7 added for FDC/Gel interface of ground electrode), incorporating the bridging FDC layer. The analysis indicates a significant decrease in the maximum electric field intensity along the lines adjacent to the SG and AlN materials of the ground electrode, as depicted in Fig. 4. This notable reduction can be attributed to the extension of the nonlinear FDC layer, which now envelops the ground electrode's TPs. By doing so, the nonlinear conductive properties of the layer over these critical regions are enhanced, particularly in areas subjected to elevated electric field stresses.

TABLE III. Electric Field Along Lines For Section IV

E_{max} (kV/mm)	Freq. (kHz)	L1	L2	L3	L4	L5	L6	L7
Unipolar	60×10^{-3}	11.81	11.94	11.74	24	13.34	23.55	20.09
	1	13.48	14.9	14.51	24.76	15.7	24.75	19.13
	10	17.12	17.4	15.24	24.88	18.2	26.56	18.37
	50	19.13	18.52	16.86	25.02	19.74	27.34	17.87
	100	20.68	20.79	19.06	24.64	20.29	27.63	17.63
	500	21.39	21.58	21.69	25.55	21.06	28.44	17.26
Bipolar	60×10^{-3}	12.69	12.64	14.05	25.82	14.33	23.95	20.12
	1	14.56	15.44	15.25	26.19	16.02	25.11	19.21
	10	21.23	21.52	21.43	28.32	19.93	26.94	18.65
	50	21.55	21.92	21.76	28.87	20.54	27.53	18.41
	100	21.94	22.54	21.81	28.94	21.56	28.01	17.75
	500	22.94	23.21	21.97	29.49	21.45	28.25	17.22

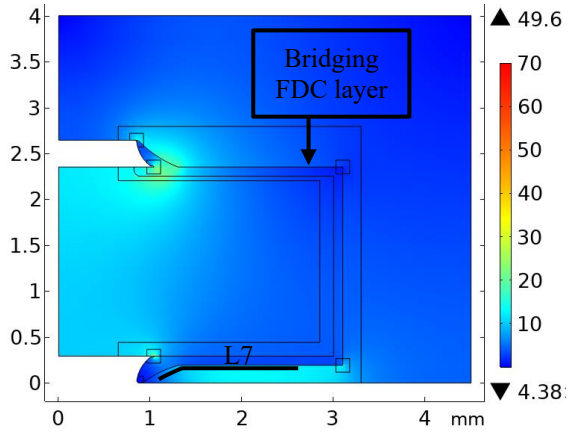

Fig 4. Electric field distribution for nonlinear bridging FDC layer (500 kHz).

Furthermore, the findings reveal that the electric field values associated with the bridging FDC layer scenario exhibit higher intensities for bipolar square voltages than unipolar across all frequencies. The electric field for lines L3 and L4 is reduced by 72.28% and 43.89% for unipolar and 66.86% and 39.70% for bipolar square voltage under 60 Hz. At 500 kHz, the electric field reduction is also significant, decreasing by 42.85% and 33.36% for unipolar and by 41.96% and 22.86% for bipolar square wave voltages, as depicted in Fig. 5. It is noteworthy that a high electric field previously observed near the TPs of the ground electrode is now lower than the HV electrode. The increase in electric field at the TPs of the HV electrode also remains minimal compared to the nonbridging layer.

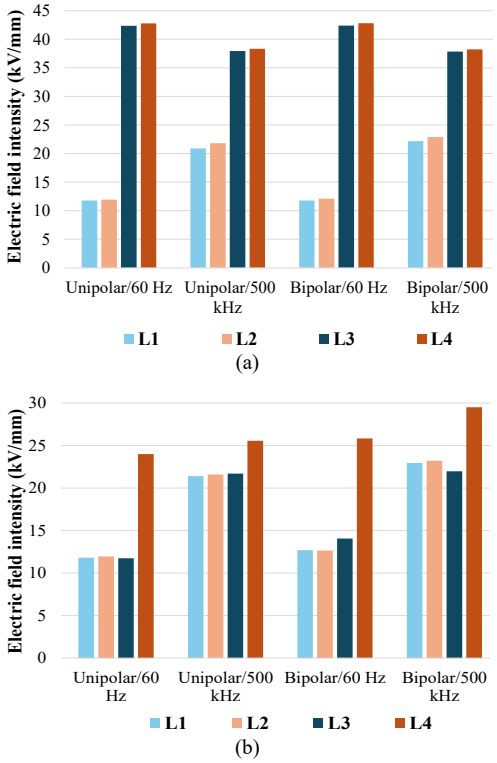

Fig 5. Comparison of electric field intensities for two different strategies: (a) nonlinear nonbridging FDC layer, (b) nonlinear bridging FDC layer.

V. Impact of Ceramic Substrate Thickness on Electric Field Reduction

Several geometric strategies have been explored to mitigate the high electric field concentration around TPs in WBG power modules. Among these are increasing the ceramic substrate thickness, introducing metal layer offsets, and using protruding substrates [36, 37]. Metal layer offsets can reduce the electric field in one region, but often at the expense of increasing it elsewhere. The protruding substrate method was excluded as it requires altering the geometry of the metal electrodes—which is relatively complex. Increasing the ceramic substrate thickness, on the other hand, offers a more straightforward solution [38]. Since the electric field is inversely proportional to the distance between electrodes, a thicker ceramic layer helps in reducing field intensity. However, exceeding standard thickness limits can introduce manufacturing challenges, as most substrate providers have maximum allowable ceramic thicknesses. Thicker substrates also raise thermal resistance, compromising thermal performance and increasing the overall size and cost of the module. Considering these factors, the ceramic thickness in this simulation varied from 2.06 to 2.56 and 2.86 mm without exceeding these limits. The model's overall dimensions remain the same; therefore, the power module size is not increased.

A. 2.56 mm Substrate Thickness

Fig. 6 illustrates the influence of frequency and voltage polarity on the peak electric field observed in the HV AlN substrate for a nonlinear FDC layer with a substrate thickness of 2.56 mm. Fig. 8 presents similar trends observed in other TP regions. Increasing the substrate thickness by 0.5 mm also extends the FDC layer length, reducing the switching field (E_b) from 4 to 3.75 kV/mm. The graphs show that the electric field stress along the measuring lines is consistently lower for the 2.56 mm ceramic substrate than the 2.06 mm case. Furthermore, the electric field intensity is always higher for bipolar square voltage than unipolar. For instance, when the substrate thickness increases from 2.06 mm to 2.56 mm, the highest electric field intensity for bipolar voltage reduces by 8.46%, 8.92%, 8.51%, 8.14%, 8.16%, 9.73%, and 11.44% along the seven measuring lines, respectively. In the case of unipolar voltage, the reductions are 6.92%, 5.38%, 9.22%, 9.86%, 6.51%, 16.49%, and 11.88%, respectively. When comparing the highest electric field between unipolar and bipolar square voltages, the maximum electric field along the SG and AlN regions is found to be 14.99% and 5.19% higher, respectively, for 500 kHz and 9.98% and 6.08% higher, at 100 kHz. A similar trend is observed across other frequencies when comparing electric fields for unipolar and bipolar square voltages at 2.56 mm thickness. This trend also aligns with the comparison between the results in Fig. 8 for the 2.56 mm case and those in Table III for the 2.06 mm case.

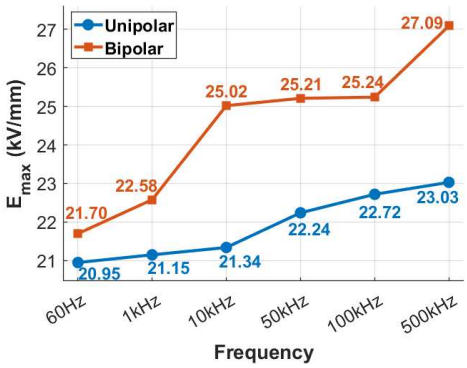

Fig 6. Maximum electric field trend along L4 for 2.56 mm substrate thickness.

B. 2.86 mm Substrate Thickness

In this section, the substrate thickness is further increased to 2.86 mm, which represents the maximum practical limit. Increasing the thickness beyond this point is not feasible for two reasons: (1) the additional reduction in electric field becomes very low, and (2) the thermal drawbacks introduced by the thicker substrate outweigh the benefits [39]. Fig. 7 illustrates the effect of frequency and voltage polarity on the peak electric field intensity in the TP areas of the HV AlN substrate for a substrate thickness of 2.56 mm, while Fig. 9 shows similar trends observed in other TP regions. Notably, further increasing the substrate thickness by 0.5 mm reduces E_b to 3.6 kV/mm. The graphs reveal that electric field stress along the measuring lines is consistently lower for the 2.86 mm substrate compared to 2.56 mm. The electric field intensity is also consistently higher under bipolar square voltage than unipolar square voltage. When the substrate thickness increases from 2.56 mm to 2.86 mm, the highest electric field intensity for bipolar voltage reduces by 5.48%, 4.26%, 3.13%, 11.81%, 3.69%, 9.73%, and 7.15% along the seven measuring lines, respectively. In the case of unipolar voltage, the reductions are 8.54%, %, 9.30%, 33.21%, 2.91%, 5.59%, 6.65%, and 6.9%, respectively. When comparing between unipolar and bipolar square voltages, the maximum electric field along the SG and AlN regions is found to be 6.4% and 8.26% higher, respectively, for 500 kHz and 18.42% and 7.93% higher, at 100 kHz. A similar trend is observed across other frequencies when comparing electric fields for unipolar and bipolar square voltages at 2.86 mm thickness. This trend also aligns with the comparison between the results in Fig. 9 for the 2.86 mm case and those in Fig. 8 for the 2.56 mm case.

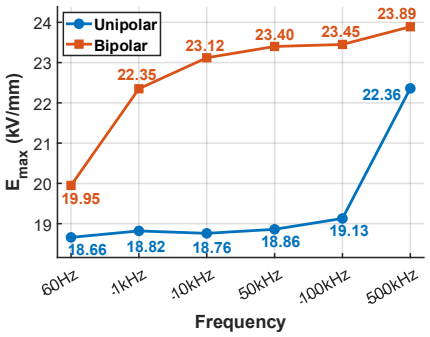

Fig 7. Maximum electric field trend along L4 for 2.86 mm substrate thickness.

An important observation from Figs. 8 and 9, as well as Tables II and III, show that the electric field remains relatively low, up to 10 kHz. However, once the square wave frequency reaches 10 kHz, there is a sudden and steep rise in electric field intensity compared to the previous case at 1 kHz. Beyond 10 kHz, although the frequency continues to increase, the rise in the electric field becomes much less pronounced. In summary, the current mitigation strategies appear effective for square wave operation up to 10 kHz, but beyond this point, the electric field stress begins to exceed the insulation strength of typical materials. This behavior can be attributed to the nature of the applied voltage: previous studies were primarily focused on DC or sinusoidal AC voltages [40], where neither frequency effects nor steep rise times were present. In contrast, square wave voltages with high frequencies and fast rise times, such as the 500 kHz and 175 ns rise time used in this study, consistently intensify electric field stress, especially near the TPs in power module packages. Despite these challenges, when comparing the electric field stress of the conventional model (Table I) with the optimized configurations presented in Figs. 7 and 9, it is evident that using a nonlinear FDC layer combined with increased ceramic substrate thickness significantly reduces the electric field at low frequencies (e.g., 60 Hz) and high frequencies (100 kHz and 500 kHz). Future work will explore integrating innovative encapsulation materials alongside these existing strategies to mitigate electric field stress.

VI. Conclusion

This research addresses the critical challenge of mitigating high electric field stress in (U)WBG power modules operating under high-frequency fast rise square voltages. A comparative analysis was done to evaluate the efficacy of nonlinear FDC layers under unipolar and bipolar square wave conditions. Results show that bipolar square voltages consistently produce higher electric field stress than unipolar ones, making the disparity more pronounced at elevated frequencies. The study reveals that non-bridging FDC layers reduce electric field near HV electrodes but shift the stress toward ground electrodes.

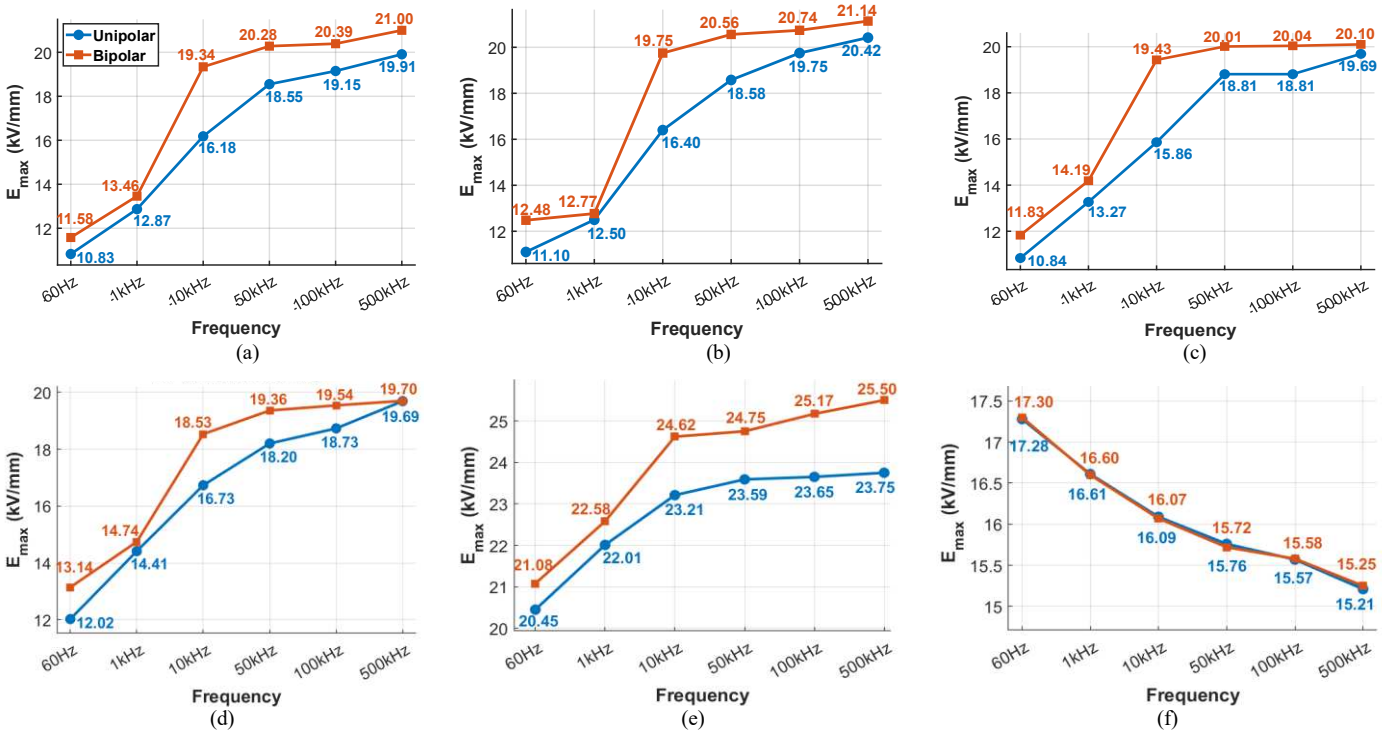

Fig 8. Maximum electric field trend for 2.56 mm substrate thickness along: (a) Line L1, (b) Line L2, (c) Line L3, (d) Line L5, (e) Line L6, (f) Line L7.

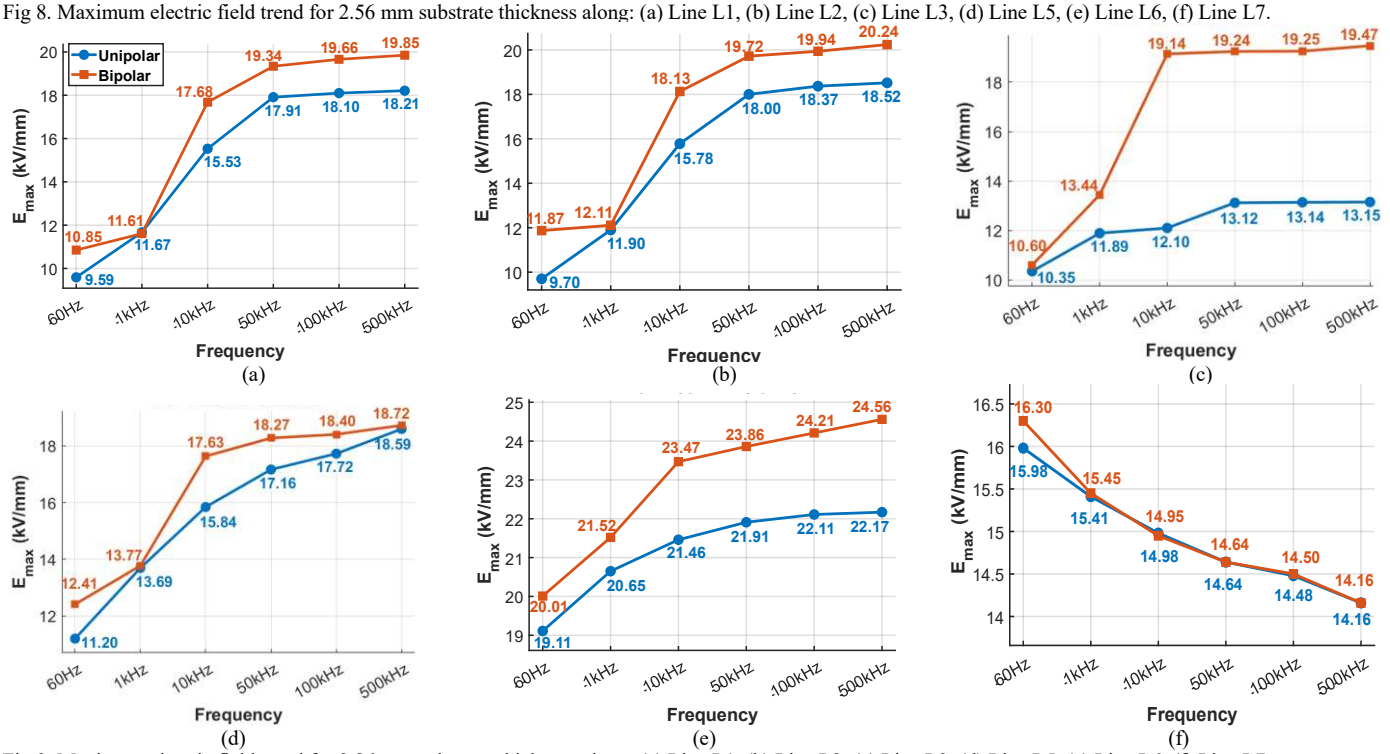

Fig 9. Maximum electric field trend for 2.86 mm substrate thickness along: (a) Line L1, (b) Line L2, (c) Line L3, (d) Line L5, (e) Line L6, (f) Line L7.

In contrast, bridging FDC layers effectively reduces stress across both electrodes. The key contribution of this study lies in the empirical validation of FDC layer performance under high-frequency, fast-rise square wave excitation—an operational condition closely aligned with real-world (U)WBG power module applications that have been largely overlooked in existing literature. The electric field results for different cases under various frequencies further demonstrate that while the efficacy of nonlinear FDC layers diminishes with increasing frequency, they remain substantially more effective than conventional designs. Additional electric field stress mitigation can be achieved by increasing ceramic substrate thickness from 2.06 mm to 2.86 mm, although considerations must be made for thermal stress. To the best of the author's knowledge, this study is the first to investigate the influence of square waveform polarity through mathematical modeling. These findings

provide a strong foundation for the design of more reliable high-power-density (U)WBG power electronic modules.

REFERENCES

[1] P. Adhikari and M. Ghassemi, "A comprehensive review of mitigation strategies to address insulation challenges within high-voltage, high-power-density (U)WBG power module packages," *IEEE Trans. Dielectr. Electr. Insul.*, vol. 31, no. 5, pp. 2676-2700, Oct. 2024.

[2] P. Adhikari and M. Ghassemi, "Navigating strategies to mitigate insulation issues within high power density (U)WBG power module packages: A comprehensive review emphasizing alternative encapsulation materials," *IEEE Trans. Ind. Appl.*, vol. 61, no. 2, pp. 3337-3358, March-April 2025.

[3] P. Adhikari, B. Adhikari, E. Arafat, and M. Ghassemi, "Comparative analysis of partial discharge phenomena in silicone gel under DC voltage utilizing optical and electrical techniques for (U)WBG power module applications," *IEEE Trans. Dielectr. Electr. Insul.*, *Early Access*.

[4] S. K. Mazumder *et al.*, "Overview of wide/ultrawide bandgap power semiconductor devices for distributed energy resources," *IEEE J. Emerg. Sel. Top. Power Electron.*, vol. 11, no. 4, pp. 3957–3982, Aug. 2023.

[5] G. Iannaccone, C. Sbrana, I. Morelli, and S. Strangio, "Power electronics based on wide-bandgap semiconductors: Opportunities and challenges," *IEEE Access*, vol. 9, pp. 139446-139456, 2021.

[6] P. Adhikari and M. Ghassemi, "Electric field mitigation in (U)WBG power module using nonlinear field-dependent conductivity layer and protruding substrate under high-frequency, high-slew-rate square wave voltages," *IEEE Trans. Dielectr. Electr. Insul., Early Access*.

[7] B. Zhang *et al*., "Dielectric properties characterization and evaluation of commercial silicone gels for high-voltage high-power power electronics module packaging," *IEEE Trans. Dielectr. Electr. Insul.*, vol. 30, no. 1, pp. 210-219, Feb. 2023.

[8] L. Wang, Z. Zeng, P. Sun, S. Ai, J. Zhang, and Y. Wang, "Electric-field-dominated partial discharge in medium voltage SiC power module packaging: model, mechanism, reshaping, and assessment," *IEEE Trans. Power Electr.*, vol. 37, no. 5, pp. 5422-5432, May 2022.

[9] X. Li *et al*., "A 10 kV SiC MOSFET power module with optimized system interface and electric field distribution," *IEEE Trans. Power Electr.,* vol. 39, no. 8, pp. 9540-9553, Aug. 2024.

[10] L. Zheng, S. Ji and X. Yao, "A Review of High Voltage Challenges and Developments of Power Electronics Packaging," in *Proc. Int. Power Modulator and High Voltage Conf. (IPMHVC)*, 2024, pp. 1-4.

[11] B. Zhang *et al*., "Electrical properties of silicone gel for WBG-based power module packaging at high temperatures," *IEEE Trans. Dielectr. Electr. Insul.*, vol. 30, no. 2, pp. 852-861, Apr. 2023.

[12] M. M. Tousi and M. Ghassemi, "Nonlinear field dependent conductivity materials for electric field control within next-generation wide bandgap power electronics modules," in *Proc. IEEE Electr. Insul. Conf. (EIC)*, 2019, pp. 63-66.

[13] M. M. Tousi and M. Ghassemi, "Electric field control by nonlinear field dependent conductivity dielectrics characterization for high voltage power module packaging," in *Proc. IEEE Int. Workshop on Integrated Power Packaging (IWIPP)*, 2019, pp. 54-58.

[14] Y. Sun, Z. Yuan, Z. Huang, J. Hu, J. He, and Q. Li, "How do the non-linear I–V curves of ZnO-based adaptive composites behave with electrodes placed on the opposite sides with a series of horizontal distances?", *High Volt.*, vol. 9, no. 5, pp. 981–988, 2024.

[15] N. Wang, I. Cotton, J. Robertson, S. Follmann, K. Evans, and D. Newcombe, "Partial discharge control in a power electronic module using high permittivity non-linear dielectrics," *IEEE Trans. Dielectr. Electr. Insul.*, vol. 17, no. 4, pp. 1319–1326, Aug. 2010.

[16] P. Adhikari and M. Ghassemi, "Alternative encapsulation material combined with geometric techniques for electric field mitigation within (U)WBG packages under high frequencies," in *Proc. Int. Power Modulator and High Voltage Conf. (IPMHVC)*, 2024, pp. 1-4.

[17] H. Reynes, C. Buttay, and H. Morel, "Protruding ceramic substrates for high voltage packaging of wide bandgap semiconductors," *Workshop Wide Bandgap Power Devices Appl. (WiPDA)*, 2017, pp. 404–410.

[18] Q. Wang *et al.*, "Tailoring electric field distortion in high-voltage power modules utilizing epoxy resin/silicon carbide whisker composites with field-dependent conductivity," *ACS Appl. Electron. Mater.*, vol. 4, no. 1, pp. 478–493, Jan. 2022.

[19] X. Chen *et al*., "Enhancement of electrical properties by including nano-aluminum nitride to micro-silicon carbide/silicone elastomer composites for potential power module packaging applications," *J. Mater. Sci., Mater. Electron.*, vol. 33, no. 23, pp. 18768–18785, Aug. 2022.

[20] P. Adhikari and M. Ghassemi, "A review of insulation challenges and mitigation strategies in (U)WBG power modules packaging," in *Proc. IEEE Texas Power Energy Conf. (TPEC)*, 2024, pp. 1–6.

[21] D. D'Amato *et al*., "Impact of PWM voltage waveforms in high-speed drives: a survey on high-frequency motor models and partial discharge phenomenon," *Energies*, vol. 15, no. 4, pp. 1406–1406, Feb. 2022.

[22] S. Wang *et al.*, "Effect of air gap on electrical tree in epoxy resin under high frequency bipolar square-wave voltage," *Materials*, vol. 13, no. 24, Art. no. 24, Jan. 2020.

[23] M. Yang and B. T. Phung, "Motor winding insulation degradation under repetitive voltage pulses," *IEEE Access*, vol. 12, pp. 77658–77674, 2024.

[24] C. Zhang *et al.*, "Electrical treeing failure in silicone gel insulation for encapsulation under high frequency bipolar square-wave voltage," *Eng. Fail. Anal.*, vol. 148, p. 107092, Jun. 2023.

[25] S. S. Linn and L. Zhu, "Dielectric breakdown testing of insulation materials under high-frequency bipolar square wave voltage by repetitive pulses," *Int. J. Sci. Res. Publ.*, vol. 13, no. 10, pp. 124–129, Oct. 2023.

[26] L. Elorza Azpiazu, G. Almandoz, A. Egea, G. Ugalde, and X. Badiola, "Study of partial discharge inception voltage in inverter fed electric motor insulation systems," *Appl. Sci.*, vol. 13, no. 4, Art. no. 4, Jan. 2023.

[27] M. Ishiko, "Recent R&D activities of power devices for hybrid electric vehicles," *RD Rev. Toyota CRDL*, vol. 39, Jan. 2004.

[28] https://webstore.iec.ch/en/publication/5113.

[29] Z. Zhang *et al.*, "Package design and analysis of a 20-kV double-sided silicon carbide diode module with polymer nanocomposite field-grading coating," *IEEE Trans. Compon. Packag. Manuf. Technol.*, vol. 14, no. 5, pp. 776–783, May 2024.

[30] C. B. O'Neal, Z. Cole, J. Stabach, G. Falling, P. Killeen, and B. Passmore, "Compact, high-temperature, single-level power modules for 10 to 25 kV DC link voltages using silicon carbide power electronics," in *Proc. Int. Workshop Integr. Power Packaging (IWIPP)*, May 2015, pp. 127–130.

[31] L. Donzel, F. Greuter, and T. Christen, "Nonlinear resistive electric field grading Part 2: Materials and applications," *IEEE Electr. Insul. Mag.*, vol. 27, no. 2, pp. 18–29, Mar. 2011.

[32] M. Chen, Y. Wang, Y. Ding, L. Fan and Y. Yin, "Self-Adaptive field-grading coating for partial discharge mitigation of high voltage power module under high dv/dt square wave voltage," *IEEE Trans. Power Electron.*, vol. 39, no. 8, pp. 9079-9083, Aug. 2024

[33] M. M. Tousi and M. Ghassemi, "Electrical insulation packaging for a 20 kV high density wide bandgap power module," in *Proc. IEEE Energy Conversion Congress and Exposition (ECCE)*, 2019, pp. 4162-4166.

[34] P. Adhikari and M. Ghassemi, "Characterizing nonlinear field dependent conductivity layers to mitigate electric field within (U)WBG power modules under high frequency, high slew rate square voltage pulses," in *Proc. IEEE Texas Power Energy Conf. (TPEC)*, 2024, pp. 1-6.

[35] C. Zhang *et al.*, "Effect of bipolar square wave voltage with varied frequencies on electrical tree growth in epoxy resin," *IEEE Trans. Dielectr. Electr. Insul*., vol. 28, no. 3, pp. 806-814.

[36] L. Wang et al., "A review of partial discharge in medium voltage SiC power modules under square wave excitation: Characterization, mitigation, and detection," *IEEE Trans. Power Electron*., vol. 12, no. 4, pp. 3588–3606, Aug. 2024.

[37] Z. Huang, C. Chen, Y. Kang, S. Munk-Nielsen, and C. Uhren-feldt, "Mitigation measures of the electric field in the medium-voltage power module: Effect of voltage types and recommendations for designers," *High Voltage*, vol. 6, no. 5, pp. 836–849, Oct. 2021.

[38] C. F. Bayer, E. Baer, U. Waltrich, D. Malipaard, and A. Schletz, "Simulation of the electric field strength in the vicinity of metallization edges on dielectric substrates," *IEEE Trans. Dielectr. Electr. Insul*., vol. 22, no. 1, pp. 257-265, Feb. 2015.

[39] X. Li *et al*., "A 10 kV SiC power module stacked substrate design with patterned middle-layer for partial discharge reduction," *in Proc. IEEE Applied Power Electron. Conf. and Expo. (APEC)*, Orlando, FL, USA, 2023, pp. 344-349.

[40] K. Li, B. Zhang, X. Li, F. Yan, and L. Wang, "Electric field mitigation in high-voltage high-power IGBT modules using nonlinear conductivity composites," *IEEE Trans. Compon., Packag. Manuf. Technol*., vol. 11, no. 11, pp. 1844–1855, Nov. 2021.